Coastal aeolian sediment transport in an active bed surface layer
Tracer study and conceptual model

Uphues, Charlotte F.K.; van IJzendoorn, Christa O.; Hallin, Caroline; Pearson, Stuart G.; van Prooijen, Bram C.; Miot da Silva, Graziela; de Vries, Sierd

DOI
10.1002/esp.5449

Publication date
2022

Document Version
Final published version

Published in
Earth Surface Processes and Landforms

Citation (APA)
Uphues, C. F. K., van IJzendoorn, C. O., Hallin, C., Pearson, S. G., van Prooijen, B. C., Miot da Silva, G., & de Vries, S. (2022). Coastal aeolian sediment transport in an active bed surface layer: Tracer study and conceptual model. *Earth Surface Processes and Landforms*, *47*(13), 3147-3162. https://doi.org/10.1002/esp.5449

Received: 16 December 2021 | Revised: 7 July 2022 | Accepted: 10 July 2022

DOI: 10.1002/esp.5449

RESEARCH ARTICLE

ESPL WILEY

Coastal aeolian sediment transport in an active bed surface layer: Tracer study and conceptual model

Charlotte F. K. Uphues[1,2] | **Christa O. van IJzendoorn**[1] | **Caroline Hallin**[1,3] | **Stuart G. Pearson**[1,4] | **Bram C. van Prooijen**[1] | **Graziela Miot da Silva**[2] | **Sierd de Vries**[1]

[1]Faculty of Civil Engineering and Geosciences, Delft University of Technology, Delft, The Netherlands

[2]Beach and Dune Systems (BEADS) Laboratory, College of Science and Engineering, Flinders University, Adelaide, South Australia, Australia

[3]Division of Water Resources Engineering, Faculty of Engineering, Lund University, Lund, Sweden

[4]Deltares, Department of Applied Morphodynamics, Delft, The Netherlands

Correspondence
Charlotte F. K. Uphues, Beach and Dune Systems (BEADS) Laboratory, College of Science and Engineering, Flinders University, Sturt Road, Bedford Park South Australia 5042, Australia.
Email: uphu0001@flinders.edu.au

Abstract

Coastal aeolian sediment transport is influenced by supply-limiting factors caused by sediment sorting by grain size. Sorting processes can lead to coarsening of the bed surface and influence the formation of aeolian ripples. However, the influence sorting processes and bedforms might have on the magnitude of the transport is not fully understood. This study explores sorting processes and their influence on the magnitude and mode of aeolian transport by using sediment tracers. Sand was painted in different colors according to particle size and placed on a supratidal beach in Noordwijk, the Netherlands. Several experiments were conducted with varying wind speeds. Surface sampling and cameras tracked the sand color movement on the bed surface, and wind velocity was measured. The tracer experiments showed that ripples developed in moderate wind conditions. Once the ripples had formed, the supply of finer tracer grains in the downwind direction decreased over time, while the supply of coarser grains remained constant. A linear relationship between ripple migration speed and wind speed was found. For higher wind speeds, no ripples or differences in transport of grain size fractions were observed. Instead, alternating phases of erosion and deposition of the bed surface were observed, which could not be related to local variations in wind velocity. Based on these results and literature, a conceptual model was developed for an active bed surface layer with two transport regimes corresponding to moderate (I) and high (II) wind speeds. The conceptual model is intended to guide the selection of aeolian sediment transport models as a function of wind speed, bed characteristics, and upwind sediment supply. For Regime I, transport could be modeled using a linear relationship between sediment transport and wind speed and for Regime II using a third power relationship in combination with a process-based model accounting for supply limitations.

KEYWORDS
aeolian ripples, armoring, beach, field measurements, particle tracing, sediment sorting, supply limited

1 | INTRODUCTION

Estimates of aeolian sediment transport rates are crucial for making long-term predictions of the evolution of dune morphology. Detailed numerical models for aeolian transport are commonly based on equilibrium transport equations relating the transport rate to the wind speed following third-power relationships (e.g., Bagnold, 1937; Hsu, 1971; Kawamura, 1951; Lettau & Lettau, 1978; Owen, 1964;

Sørensen, 2004; Zingg, 1953). These equations were developed in lab and desert studies with abundant sediment supply. When applied in coastal environments, however, the transport rates are commonly overestimated (Barchyn et al., 2014; Kroon & Hoekstra, 1990; Sarre, 1989; Sherman & Li, 2012; Sherman et al., 1998). Supply-limiting processes, such as sediment sorting, soil moisture, and armor layer development, hamper the predictive capability of equilibrium transport relationships (e.g., de Vries et al., 2014; Hoonhout & de Vries, 2016). In particular, the potential role of the interplay between aeolian transport, sediment sorting, and bedforms on the total transport rates is not yet well understood. A better understanding of these processes is needed to improve estimates of aeolian sediment transport rates and thus numerical predictions of the morphological evolution of beaches and dunes.

In this paper, we focus on non-suspended aeolian sediment transport, erosion, and deposition occurring at or near the bed surface. Sediment transport occurs whenever there are winds of sufficient strength and granular material available for erosion (Bagnold, 1941). When the shear stress at the bed becomes larger than the gravity and inter-particle forces of the bed particles, the bed particles are eroded, and sediment transport is initiated. Bagnold (1937) classified three different aeolian transport modes: creep, saltation, and suspension (Figure 1). Sand-sized particles (63 μm to 2 mm) are commonly transported along the surface in the form of creep or saltation. Creep is the movement of grains in continuous or near-continuous contact with the sand bed (Walker, 1981) and saltation is the wind-driven lift-off, hopping, and splashing of particles, following long, parabolic trajectories (Bagnold, 1937). Lighter particles are transported in suspension, in which they can be kept aloft for relatively long distances due to the turbulence of the air (Anderson, 1986; Bagnold, 1937; Pähtz et al., 2014; Tsoar & Pye, 1987). In sandy coastal environments, creep and saltation are the dominating aeolian transport processes.

The potential total sand transport rate, q_{cap}, including sand transport in the form of creep, saltation and suspension, can be described as a result of the momentum transfer from the wind to the sediment (Bagnold, 1937):

$$q_{\mathrm{cap}} = C_b \sqrt{\frac{d}{D}} \frac{\rho}{g} u_*^3, \tag{1}$$

where C_b is a constant of 1.8 for naturally graded sand, d is grain diameter and D is a reference grain diameter, typically 0.25 mm, ρ is the air density, g is the gravitational acceleration, and u_* is the shear velocity. q_{cap} is the sediment transport capacity by the wind when the supply of erodible sediment is unlimited.

On beaches, the transport capacity is limited by bed properties like surface moisture (Davidson-Arnott et al., 2005; Schmutz & Namikas, 2018) and grain size sorting (Hoonhout & de Vries, 2016), morphological properties like beach slope (de Vries et al., 2012; Hardisty & Whitehouse, 1988) and fetch length (Bauer & Davidson-Arnott, 2003), and/or the presence of physical obstructions like vegetation (Buckley, 1987) or lag deposits (de Vries et al., 2014; van der Wal, 1998). These supply limitations are commonly accounted for by modifying the empirical calibration parameter in the third-power equations (Houser, 2009; Nickling & Davidson-Arnott, 1990). The results of the equations are partly successful, with most equations overestimating measured aeolian transport rates depending on calibration and the field data used (see Sherman & Li, 2012; Sherman et al., 2013). Generic methods to derive calibration parameters are unavailable, and the lack of process descriptions limits the predictive ability (Sherman & Li, 2012).

Process-based simulations of sediment sorting have proven to require multi-fraction approaches to simulate transport of different grain sizes, representing the grain size distributions in the field (Hoonhout & de Vries, 2016). Grain size selective erosion, transport, and deposition can result in a coarsening of the bed surface, often referred to as armoring (e.g., Bagnold & Taylor, 1937; Hirano, 1971; Hoonhout & de Vries, 2016). Armour layers decrease the total transport because the surface particles available for transport tend to be coarser and more difficult to move. They are, therefore, a physical limit on the transport capacity. Transport of differently sized grains can also cause very local deposition and erosion at the bed surface, leading to the formation of ripples (Bagnold, 1941; Wang et al., 2019; Wilson, 1972). Aeolian ripples are characteristic bedforms for many sandy environments. Sand transport by saltation influences their development and migration (Bagnold, 1941; Sharp, 1963; Sherman et al., 2019). Coarse and fine grains show different transport trajectories, typically resulting in deposition of coarser grains at the ripple crests and finer grains in the ripple troughs (Anderson & Bunas, 1993; Bagnold, 1941; Wang et al., 2019). Ripples primarily transport sediment in the form of creep (Sharp, 1963). The creep transport rates associated with ripple migration have been related to the total sediment transport rates (Sherman et al., 2019). Still, it is not fully understood what influence and importance aeolian ripple formation and propagation have on the erosion, deposition, and magnitude of aeolian sediment transport. The interaction between aeolian bedform dynamics and grain-size-selective transport has not yet been clarified.

Field measurements are essential for explaining aeolian transport processes. Point measurements of wind speed and proxies of sediment fluxes are often collected to derive/validate relationships between sediment fluxes and the local wind speed (e.g., Davidson-Arnott et al., 2005; de Vries et al., 2014; Hoonhout & de Vries, 2017). However, wind speed and sediment transport measured with point measurement methods such as cup, vane, or sonic anemometers and

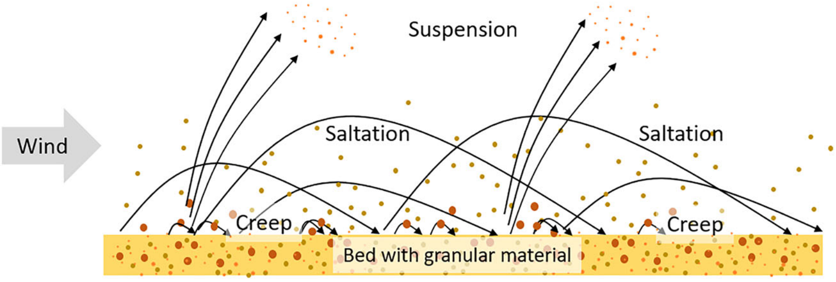

FIGURE 1 Schematic of aeolian sediment transport modes according to Bagnold (1937): creep, saltation, and suspension. Grains of different sizes (brown = coarsest grains, beige = medium grains, and orange = finest grains) interact with the wind (represented as a gray arrow). Thin black arrows denote typical particle trajectories associated with each mode of transport

sediment traps, saltiphones, or laser sensors, respectively, only give an indication of transport at one location (Black et al., 2017; van Rijn, 2019; White, 1998). They do not provide information on the spatial patterns of wind speed or sediment particle transport. Compared to point measurements, particle tracing (or particle/sediment tracking) can provide additional spatial and temporal insights into sediment transport, erosion, and deposition near the bed surface. Particle tracing is a field method where grains are labeled or tagged and then allowed to disperse naturally with ambient currents (Black et al., 2007). The dispersal of the tracer can then be estimated based on the recovered particles complementing point measurement methods (Wang et al.2017).

Tracer studies have been carried out in various coastal environments. For subaerial coastal environments, most tracer experiments have been conducted in the intertidal area (e.g., Kato et al., 2014; Oliveira et al.2017; Robin et al., 2009; Silva et al., 2007; Vila-Concejo et al., 2004; Williams et al., 2003; Wright et al.2015), but mainly focused on hydrodynamic transport processes. In coastal dune areas, sediment tracer studies have been applied to compare observed tracer sediment transport rates with theoretical models (Berg, 1983) and with experimentally estimated sand trap transport rates (Cabrera & Alonso, 2010). To the best of our knowledge, no previous studies have applied tracers on beaches to investigate the small-scale processes of the interplay between the wind, erosion, and deposition at the bed, sediment transport of differently sized grains, and supply limitations. Possible reasons for this could be that aeolian sediment transport is usually less restricted compared to hydrodynamic sediment transport (Wang et al., 2017), which makes it harder to track the particle movement and to define sampling areas. Furthermore, wind-blown sand grains tend to move more quickly than water-driven sand grains (Pähtz et al., 2020), resulting in a much faster redistribution of tracer particles, which can make it difficult to retrieve individual tracer grains in the field.

In this paper, we use tracers to study the interaction between deposition, erosion, bedform dynamics, and aeolian transport for differently sized sand grains to improve our understanding of aeolian grain-size-selective transport on beaches. Furthermore, we propose a conceptual framework for modeling aeolian transport, erosion, and deposition at the bed surface, which helps to better quantify aeolian sediment transport. Fieldwork using tracers is carried out at the supratidal, well-graded sandy beach in Noordwijk, the Netherlands. Multi-fraction sediment transport and bedform development are studied for varying wind speeds using a novel grain counting approach based on imagery. The tracer study results and previous research within this field are integrated into a conceptual model framework intended to guide the selection of transport equations for different wind and grain size conditions.

2 | METHODS

A tracer study was employed to observe how distinct grain sizes are transported in the interface area between the bed and the moving air by coastal aeolian sediment transport processes. A field site in the Netherlands with sand-sized grains mainly exposed to oblique-to-onshore winds was chosen (Figure 3). Sand grains were painted in four different colors according to particle size to observe the spatiotemporal dispersal of the differently sized tracer grains. Two types of experiments were conducted: mixed experiments and separated experiments (Figure 2). **S**eparated experiments (**S**01–**S**03) were executed by placing two **S**eparated fractions, a coarser one and a finer one, as two adjacent stripes parallel to the wind direction. This should show whether the tracers behave as expected in aeolian beach environments—that is, whether finer grains are transported more easily than coarser grains. For this, two contrasting colors (red and green) were chosen. **M**ixed experiments (**M**01–**M**04) with **M**ixed tracer sand (1/4 of each fraction) were performed to represent the naturally occurring conditions of the native sand, which contains a range of grain sizes.

2.1 | Field site

The field site for this study was the beach of Noordwijk aan Zee, located on the central Dutch coast (Figure 3a,b). Measurements took place from 21 to 23 May 2021 at different locations in the supratidal area between the intertidal zone and the dune toe (Figure 3b). The area consists predominantly of fine quartz sand with median grain size (d_{50}) of 240 μm. The median grain size was analyzed by sieving native sediments collected from the top 3 cm (see black lines in Figure 4). The depth of 3 cm was chosen based on preliminary tests of this study, which showed that the top 3 cm are most important for grain movement. The surface sand was dry on 21 and 23 May 2021. On 22 May 2021, it was wet due to heavy rainfall before the experiment and light rainfall during the experiment. Moisture contents were not measured during the field experiments as the experiments were planned to be performed in the dry, supratidal beach area in order to reduce complexity. We still included the wet experiment on 22 May 2021 in order to discuss the effects of moisture qualitatively.

The coast of Noordwijk is wave dominated, with waves approaching the coast mainly from the SW and NNW (Quartel et al., 2007). Mean wave heights and periods along the Dutch coast are 1.2 m and 5 s, respectively, and alongshore differences in wave climate are small (Wijnberg & Terwindt, 1995). The wind climate is dominated by winds from the SW with higher average wind and gust

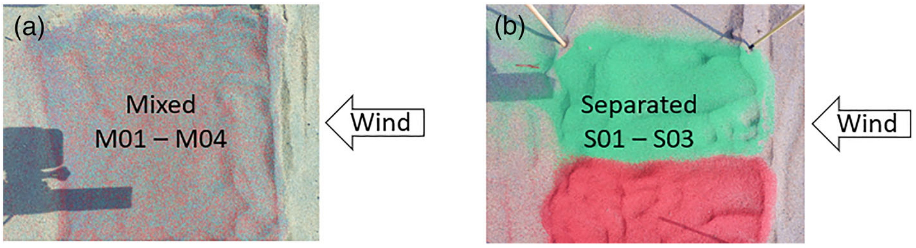

FIGURE 2 Tracer experiment types. (a) For the experiments **M**01–**M**04, **M**ixed sediment containing 1/4 of each grain-size fraction was used. (b) For the experiments **S**01–**S**03, two **S**eparated fractions, a coarser one and a finer one, placed as two adjacent stripes parallel to the wind direction were used

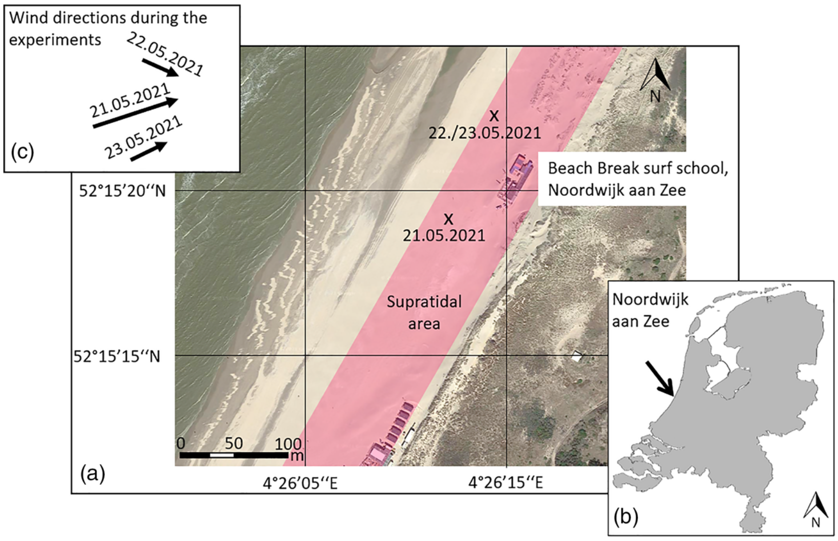

FIGURE 3 Location, orientation, and appearance of the test site in Noordwijk aan Zee. (a) Detailed top view of the location with an indication of the areas where the experiments were performed on 21 and 22/23 May 2021 and the supratidal area (red). (b) Location of the test site along the Dutch coastline. (c) Identification of the average wind velocities during the different experiments on the three days

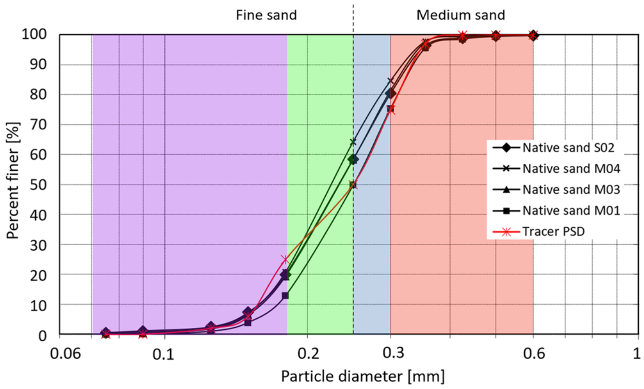

FIGURE 4 Particle size distribution (PSD) of native sand samples from the locations of the experiments M01, M03, M04, and S02 (black lines) and PSD of the tracer sand mixture which was used for experiments M01–M04 (red line) with indication of the four colors for the four different fractions

speeds during the winter months than during the summer months. The coastline is oriented SW to NE, 30° with respect to North (where the shore-normal direction is 300° with respect to North). The dominant SW winds are thus oblique onshore. The tide at Noordwijk is semi-diurnal with 1 m and 1.8 m ranges at neap and spring tide, respectively (Walstra et al., 2012). The beach slope is relatively mild, with $\tan\beta = 0.007$ (van Rijn, 2014) and the beach width varies between 100 and 200 m, depending on the tide.

2.2 | Field setup

The tracer was developed and introduced at the test site in a similar way for the **M**ixed (**M**01–**M**04) and **S**eparated (**S**01–**S**03) experiments. Native sand was sieved and colored in four different colors for four different grain size fractions (<0.18 mm, purple; 0.18–0.25 mm, green; 0.25–0.3 mm, blue; 0.3–0.6 mm, red; see Figure 4). After coloring the native sand, it was sieved for a second time to remove possible clumps. The sieves were chosen according to the particle size distribution (PSD) of the native sand so that each fraction represented approximately a quarter of the total weight. The PSD of the tracer sand mixture used for experiments M01–M04 showed a slightly larger amount of fine grains than the native sand (Figure 4). The tracer sand behaved very similar to natural sand when sieving it. Under the microscope, it could be observed that the color added only a very thin layer (which was hardly noticeable) to the native sand particles, negligible compared to the particle diameter, implying an insignificant impact on the particle weight.

On the beach, at the start of each experiment, the tracer sand was placed in an area of 30cm × 30cm, after removing a layer of native sand with similar thickness. Removing the original microtopography at the placement site allowed observation of the emergence of bedforms. After a few seconds to minutes, depending on the wind speed, the placement site adjusted to the prevailing environmental conditions and developed in a similar way to the undisturbed beach area. The dimensions of the placement area were chosen to be large enough to have a representative amount of tracer grains and small enough to perform and repeat experiments easily. The test site was protected with a removable windscreen to prevent transport of the tracer sand during preparations.

The dispersal of the tracer sand was tracked using sediment sampling and video imagery. Surface samples from the top 1 mm at different distances downwind of the placement site (see Table 1) were collected to track the horizontal movement of the sand particles. To confine the study area and obtain sufficient tracer grains in the samples, a relatively small spatial scale was chosen with sampling locations no more than 4 m downwind from the placement site. Samples were only collected when it was established visually that colored sand was transported to the sampling location. Once colored sand reached a certain location, samples were taken at this location about once every 5 min as long as colored sand was established there visually. With this method, we avoided taking many samples without a significant number of tracer particles.

Additionally, two GoPro Hero 7 cameras (A and B), looking from above, took pictures of the moving sand. Camera A observed the sediment colors present on the bed of the placement site itself, while camera B observed the sediment colors on the bed just downwind from the placement site (Figure 5a). The chosen settings for both cameras were a picture resolution of 12 megapixels (4000 × 3000 pixels),

TABLE 1 Overview of experiments executed from 21 to 23 May 2021

Experiment	Date	Start time	End time	Top view	Side view	Sample	Average wind speed (m/s)	Average wind direction (°)	Average wind shear velocity u_* (m/s)
S01	21 May 2021	15:46	16:16	✓	✓	None	15.1 (21.4)	256	1.23 (2.37)
M01	21 May 2021	17:07	17:45	✓	✓	12 at 0.5 m	15.6 (24.4)	252	1.29 (3.33)
S02	21 May 2021	18:03	18:27	✓	✓	7 at 0.5 m	15.1 (21.8)	253	1.23 (2.47)
M02	22 May 2021	15:56	17:10	✓	✓	None	7.0 (11.2)	294	0.39 (0.76)
M03	23 May 2021	13:41	14:43	✓	✓	11 at 0.5 m 10 at 2 m 7 at 4 m	8.7 (12.2)	243	0.53 (0.87)
M04	23 May 2021	15:22	16:27	✓	x	9 at 0.5 m 3 at 2 m	7.2 (10.4)	246	0.40 (0.68)
S03	23 May 2021	16:37	17:12	✓	x	None	5.9 (7.9)	252	0.31 (0.46)

Note. M indicates the experiments where a sand **M**ix of all four fractions was used, while S denotes the experiments where only two **S**eparated fractions (red and green) placed as two stripes parallel to the wind direction were used. Wind speed, direction, and wind shear velocity are averaged over the experiment duration. The wind speed/wind shear velocity (in brackets) is the maximum wind speed measured/wind shear velocity during every experiment.

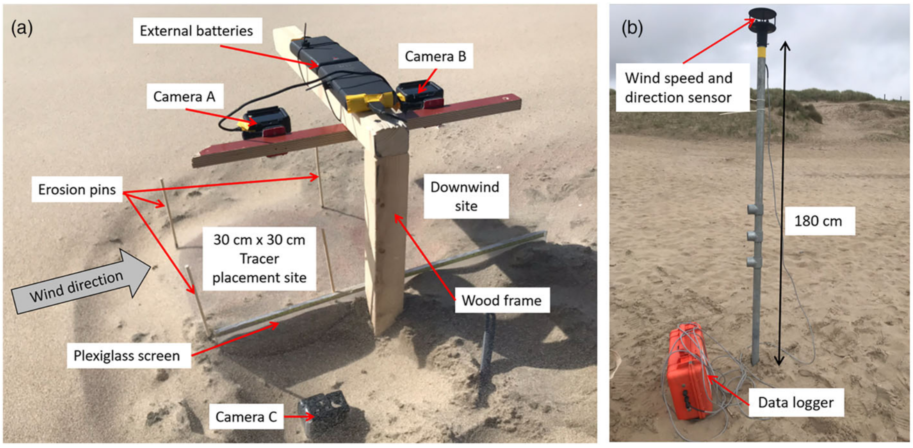

FIGURE 5 Field setup during the experiments. (a) Cameras A and B, mounted on a wooden frame and connected to external batteries, tracked the tracer movement from the top view. Camera C tracked the tracer movement through a plexiglass screen from the side view. (b) A wind speed and direction sensor was mounted to a metal pole 180 cm above the bed and connected to a data logger protected in an orange case. The device was located in proximity to the tracer placement site (between 2 and 5 m to the left or right of the placement site)

a linear field of view (FOV), and a frame rate of 1 frame per second (fps). Both cameras were mounted to a wooden frame about 20 cm above ground, taking photos of an area of about 40cm × 30cm each, which means that one pixel is of the order of 0.1 mm (about half the size of the median grain diameter). The scale in the top-view photos was obtained by taking a photo of a ruler placed on the ground at the start of each experiment. In five of the seven experiments, a third GoPro Hero 5 camera (C), with the same settings as the other two cameras, tracked the bed evolution and vertical changes in color from the side through a plexiglass screen dug into sand parallel to the mean wind direction. Measurement tape attached to the upper edge of the plexiglass screen was used to determine the scale in the side-view photos. The cameras were time synchronized by pressing the start and end buttons simultaneously. Preliminary tests showed that the cameras took the same number of images with this methodology and that the individual images were synchronized. Furthermore, moving the scaling ruler (which was visible in all cameras) in and out of the cameras at the start of every experiment provided validation of the time synchronization for each run. The placing and dimensions of the experimental setup were designed to reduce its effect on the wind field and, thus, on the sediment transport. Additionally, the bed development near the experimental setup was compared to the surrounding bed development to make sure they were similar and the effect of the setup was limited.

During all experiments, wind speed and direction were measured with a Gill 2D WindSonic ultrasonic wind speed and direction sensor (P/N:1405-PK-040) 180 cm above the bed (Figure 5b) in proximity to the tracer placement site (between 2 and 5 m to the left or right of the placement site). A HOBO Energy data logger (P/N: H22-001) logged the sensor at 0.5 Hz. Measured local wind conditions can be found in Table 1 and Figure 3c.

The wind velocities measured 180 cm above the bed were converted to an equivalent wind shear velocity at the bed. The wind shear velocity, u_*, can be derived for a given wind speed $u_w(z)$ at elevation z above ground by assuming a logarithmic profile and applying the Law of the Wall:

$$u_w(z) = \frac{u_*}{\kappa} \ln\left(\frac{z}{z_0}\right), \tag{2}$$

where κ is the von Kármán constant (0.4) and z_0 is the roughness length (Tennekes & Lumley, 1972). The saltation-induced roughness length, z_0, can be approximated by the Charnock (1955)-type model (Sherman & Farrell, 2008):

$$z_0 = \frac{Cu_*^2}{g}, \tag{3}$$

where C is the Charnock constant, with a value of 0.085 for general applications of aeolian sand transport in field settings (Sherman & Farrell, 2008).

To make our data more comparable to other studies, we decided to use the wind shear velocity at the bed, u_*, in dimensionless form, u_*/u_{*t}, inspired by the work of Sherman et al. (2019). The threshold shear velocity, u_{*t}, can be estimated by the Bagnold (1935) model:

$$u_{*t} = A\sqrt{gd\frac{\rho_s - \rho}{\rho}}, \tag{4}$$

where A is an empirical constant (0.1 for the air fluid threshold, Bagnold, 1941) and ρ_s is the grain density.

Table 1 gives an overview of all seven experiments.

2.3 | Surface sample analysis using automated counting of colored sediment

A novel method inspired by Pearson et al. (2021) was developed to count colored sediment in the surface samples automatically. All 59 collected surface samples were scanned under a Keyence VHX-5000 digital microscope (Keyence Corporation, 2014). The microscope took stitched images from every sample, which were then analyzed by a pixel color recognition algorithm counting the amount of red, green, blue, and purple pixels. A range for hue, saturation, and value/lightness (HSV/L) was defined for each color. The number of colored pixels of each color in one image was then normalized by dividing it by the total amount of colored pixels in that image. This method for analyzing the samples was chosen to overcome the tedious and time-consuming part of most historical tracer studies that visually counted the number of tracer grains in a sample, which also might be subject to human error (Black et al.2007).

Three microscope images of samples with only non-colored grains were used to test the accuracy of the pixel color recognition algorithm. In all three images, the algorithm counted about 0.1% colored pixels relative to all pixels in the image. Therefore, only images where the amount of counted, colored pixels was more than 10 times larger (>1%) were considered in the analysis, which means that we used 1% as colored pixel analysis threshold. Otherwise, the influence of the erroneously counted pixels of non-colored grains (e.g., non-colored brownish grains can have pixels that fall in the red HSV range) may become too large and distort the results.

Figure 6 shows an example of the microscope images and the pixels captured by the pixel color recognition algorithm in this image. The algorithm captures most pixels of the colored grains. However, some very dark or light pixels of the colored grains are not captured. Additionally, some pixels of non-colored grains fall in the defined HSV range of a certain color and are counted erroneously as pixels of the colored grains.

2.4 | Bed development analysis using top-view images

The top-view camera images were used to determine the change of sediment color on the bed surface. The images were edited to a time-lapse video to qualitatively describe the evolution of sediment color on the bed surface. The time-lapse videos for experiments M04 (Camera A) and S03 (Camera B) can be found at Video S1. For a more quantitative analysis, the images were post-processed using a pixel color recognition algorithm, which counted the amount of different colored pixels, similar to the algorithm used in the sediment sample analysis. The HSV ranges of the different colors were defined and tested for varying natural light conditions during the experiments to account for the different conditions in the field. This analysis worked best for the Separated experiments (with only two very distinct tracer colors) and was therefore only used in this context. The red or green pixels in a camera image counted by the algorithm were then normalized by dividing them by the total number of all pixels in that image.

Additionally, ripple characteristics were extracted from the top-view images. Ripple migration rates, u_r, were estimated by comparing the location of ripple crests in two photos taken 4 min apart from each other. The 4 min averages of ripple speed were converted to dimensionless migration rates $u_r/\sqrt{gd}$ inspired by the work of Sherman et al. (2019) and related to 4 min averages in dimensionless wind shear velocity. The averaging period of 4 min was chosen based on testing different averaging intervals using linear regression analysis, similar to the method by Sherman et al. (2019). Too-short intervals would result in small absolute measurement errors of the traveled ripple distances, which would grow into larger relative errors, and too-long intervals would mask the effects of the dynamic response of the ripples to changes in wind conditions. The same ripple crest was identified and registered in subsequent photos to provide a distance traveled, and

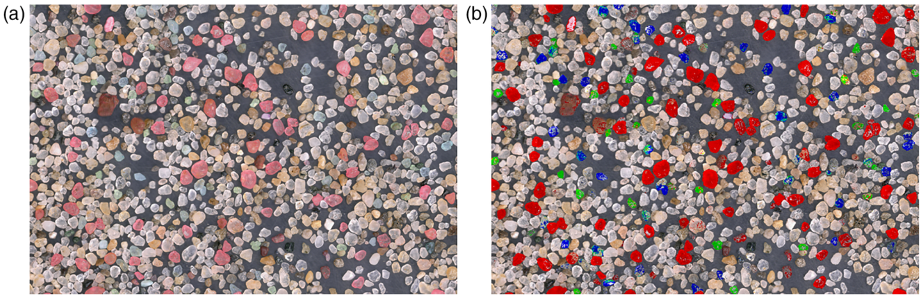

FIGURE 6 (a) Extract from a microscope image of a sample downwind of the placement site. (b) The same microscope image as in (a) but the pixels captured by the pixel color recognition algorithm are highlighted due to an increased saturation

this was converted to a migration rate using the time elapsed between images. The scaled images were also used to obtain estimates of ripple wavelength.

2.5 | Bed elevation analysis using side-view images

The side-view camera images were used to track the changes in bed elevation and volume over time. The images were edited to time-lapse videos to qualitatively describe the changes in bed elevation. The time-lapse video for experiment S01 (Camera C) can be found at Video S1. For images 1 min apart from each other, the line at the upper edge of the bed was traced. Then, the lines were compared to each other, and the area between the two lines was calculated. Intervals of erosion and deposition were identified. The influence of the plexiglass screen on the measurements was taken into account by comparing the side-view images to the top-view images, where the bed change was indicated by erosion pins. The measurements were only considered when the bed elevation close to the plexiglass was similar to the bed elevation on the other side of the test site where no plexiglass screen was placed.

3 | RESULTS

The field experiments (Table 1) display results of the mobilization and transport of different grain size fractions, ripple formation and migration, as well as alternating phases of erosion and deposition. However, one of the experiments (M02) failed to produce any useful results, as no appreciable sediment transport was observed at the tracer placement site or the beach area around. Even though the maximum measured wind speed was 11.2 m/s, the heavy rain event before and the light rain event during the experiment prevented all grains from moving.

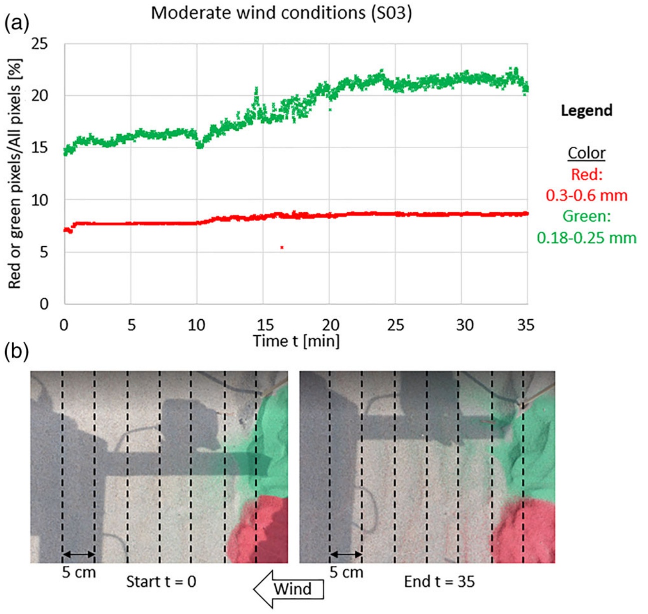

FIGURE 7 Analysis of GoPro top-view images during moderate wind conditions (S03). (a) Amount of red or green pixels relative to all pixels (12 megapixels) over time found in Camera B images. (b) Start and end Camera B image with black dashed lines indicating 5 cm scales. The smaller, green grains traveled farther than the larger, red ones, and a larger amount of green grains was mobilized

3.1 | Mobilization and sediment transport of different grain size fractions

3.1.1 | Experiments with separated sediment

The experiments with separated sediment of two grain-size fractions placed as two stripes next to each other at the test site were designed to validate the methodology with differently colored grain-size fractions and automated color recognition. During moderate wind conditions (S03), the amount of smaller, green grains that traveled in a downwind direction and the distance they traveled were larger than for the coarser red grains (Figure 7). This is represented by a relative increase of green pixels (i.e., fine grains) and an almost constant amount of red pixels (i.e., coarse grains) over time in the top-view camera images. This confirms the expectations that smaller, lighter grains are easier to mobilize by the wind than coarser grains. This indicates that for moderate wind conditions the tracer method works as expected in aeolian beach environments.

During higher wind conditions (S02), the placed tracer sand was initially partly eroded and transported away (Figure 8a). However, native sediment transported from upwind covered the remaining tracer sand and prevented it from eroding. As a result, only two out of the seven samples contained enough colored grains to include in the

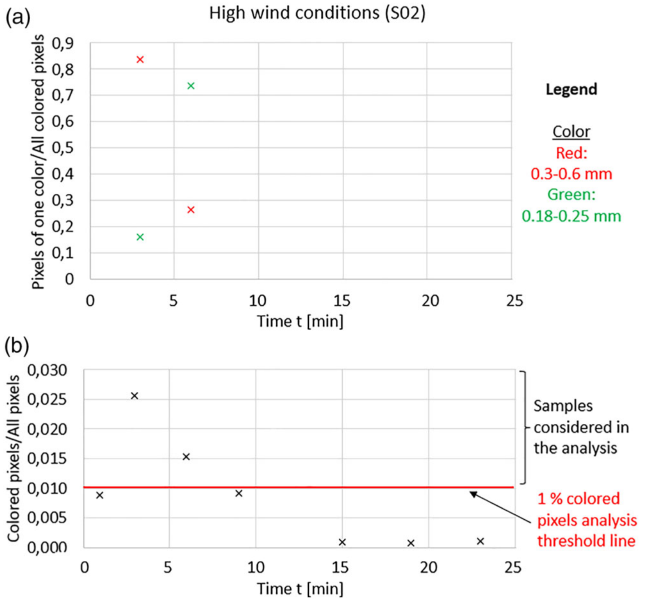

FIGURE 8 Analysis of the stitched microscope images during high wind conditions (S02). a) Normalized amount of red or green pixels relative to all colored (red and green) pixels and (b) total amount of all colored (red and green) pixels relative to all pixels over time found in the stitched images of the surface samples collected 0.5 m downwind from the placement area. In five out of seven samples (under the red 1% line), the total amount of colored pixels w.r.t. the total amount of all pixels was too small to be considered in the analysis

analysis (Figure 8b) and the tracer color movement on the bed surface was not visible in the top-view GoPro images. It is therefore not possible to trace the individual horizontal movement of the grain size fractions in this experiment.

3.1.2 | Experiments with mixed sediment

A clear signal in transport variability for differently sized grains was found for moderate wind speed (later referred to as Regime I) during M03 and M04 (Figure 9). After the mixed tracer sand was implemented, grains of all four fractions were exposed to the wind in a similar way on a flat surface. Shortly after placement, grains of all four fractions were found back in sediment samples at locations 0.5, 2, and 4 m away from the placement site (Figure 9). Over time, ripples developed, and the amount of the smaller fractions decreased (Figure 9a,c), while the amount of coarser grains stayed almost constant (relative increase of red pixels in Figure 9a,c, while the absolute number of colored pixels decreased; see Figure 9b,d). This was the case for all three locations except for the 2 m location during M04, where a slight decrease in the relative amount of red pixels over time was found. For M04, no colored sediment was observed at a 4 m distance from the placement site. For M03, there were four out of 28 samples where not enough colored pixels were found for the sample to be considered in the analysis (threshold indicated by red line in Figure 9b).

For higher wind conditions (later referred to as Regime II) during M01, one part of the initially placed tracer sand was transported relatively quickly in the downwind direction. The other part stayed at the placement site but became covered with upwind sand, which prevented the remaining tracer sand from eroding, similarly to what was observed in S02.

3.2 | Ripple migration

For moderate wind conditions (later referred to as Regime I) during M03 and M04, the formation and movement of ripples were observed (Figure 10). Ripple wavelengths varied between 4 and 10 cm, with an average length of 7 cm. For higher wind conditions (S01, S01, and

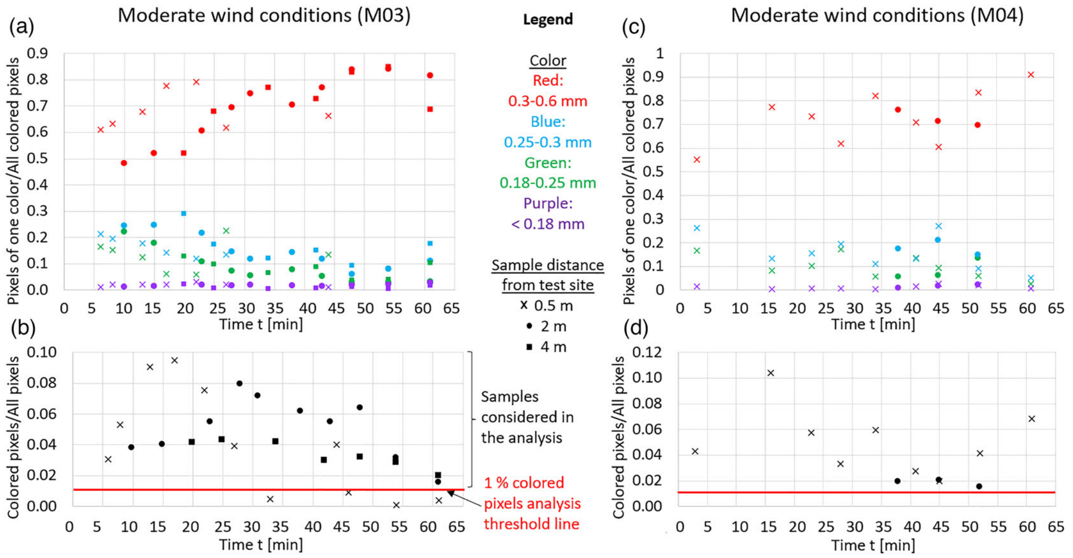

FIGURE 9 Analysis of the stitched microscope images during moderate wind conditions (M03 and M04). (a) Normalized amount of red, green, blue, or purple pixels relative to all colored (red, green, blue, and purple) pixels, and (b) total amount of all colored (red, green, blue, and purple) pixels relative to all pixels over time found in the stitched images of surface samples during experiment M03. (c,d) The same, but during M04. For samples under the red 1% line in (b) and (d), the total amount of colored pixels w.r.t. the total amount of all pixels was too small to be considered in the analysis

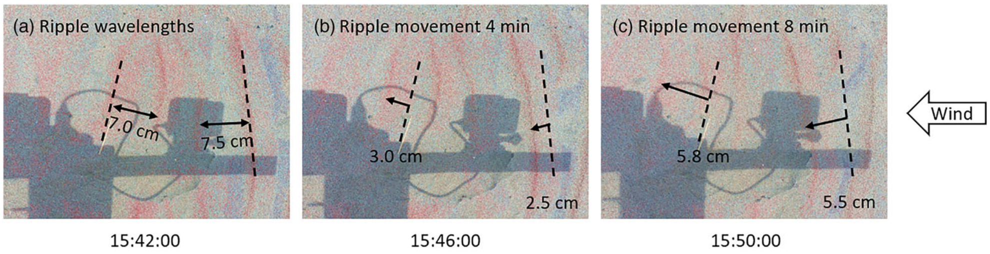

FIGURE 10 Example of ripple wavelengths and movement during moderate wind conditions (M04) observed from the top-view Camera A images. (a) Ripple wavelengths (black arrows) 20 min after the placement of the tracer sand. (b) Movement of two individual ripple crests (black arrows) within 4 min. The vertical black dashed lines indicate the position of the ripple crests at 15:42:00. (c) Movement of two individual ripple crests (black arrows) within 8 min. The vertical black dashed lines indicate the position of the ripple crests at 15:42:00

M01) and for wet sand conditions (M02), no ripples were observed at the test site or the adjacent beach area.

Figure 11 shows the dimensionless ripple migration rates, $u_r/\sqrt{gd}$, determined based on the top-view images from experiments M03 and M04 as a function of the dimensionless wind shear velocity, u_*/u_{*t}. The 31 observations of $u_r/\sqrt{gd}$ and u_*/u_{*t} are 4 min averages. From linear regression analysis, a relationship where $u_r/\sqrt{gd} = 0.0051(u_*/u_{*t} - 1.49)$ with $n = 31$ and $R^2 = 0.87$ is found. The value of 1.49 can be considered as a threshold value for ripple movement; that is, when u_*/u_{*t} exceeds 1.49, ripple movement is initiated. For dimensionless wind shear velocities above 2.1, which corresponds to measured wind speeds above 8.2 m/s at a height of 1.80 m, the linear approximation does not describe the observed variability well; several observations lie outside the upper boundary of the 90% interval. Both u_* and u_r are scaled with $\sqrt{gd}$ (see Equation 4 and Figure 11), making them no longer independent. This means that changing the grain diameter will not change the trend line, but shifts the data points along the 'expected value' line.

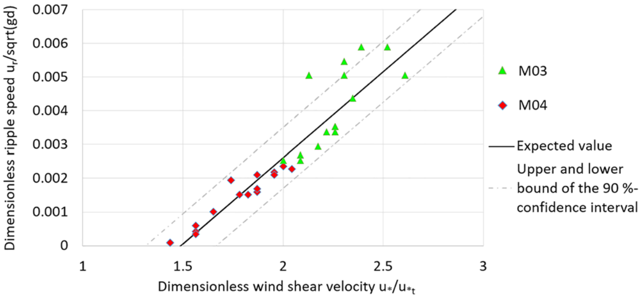

FIGURE 11 Dimensionless ripple migration rates as a function of dimensionless wind shear velocity ($n = 31$, $R^2 = 0.87$) during moderate wind conditions (M03 and M04). The solid line indicates the expected value from the regression model of all measurement points $(u_r/\sqrt{gd} = 0.0051(u_*/u_{*t} - 1.49))$. The dashed lines indicate the boundaries of the 90% confidence interval. For 10% of the measurements, the dimensionless ripple speed $u_r/\sqrt{gd}$ deviates more than 0.0009 from the expected value

3.3 | Deposition and erosion of the bed surface layer

Deposition and erosion of differently sized grains were observed in a time sequence of the camera images from the top (e.g., Figure 12) and side views. For the moderate wind conditions (later referred to as Regime I) during M03 and M04, a thin layer of mixed colored sand was initially eroded and transported in the downwind direction. The colored sediment mixture separated and ripples formed. The coarser red grains accumulated on the ripple crests, while the mix of finer (blue, green, and purple) grains accumulated in the ripple troughs. The colored sediment was slowly mixed with individual sand grains from the upwind direction which were transported on the test site. Over time, the placement site was covered by ripples propagating into the site from the upwind direction, which inhibited erosion of the remaining colored sand. From the top- and side-view images, patches of tracer sand were visible underneath the incoming ripples of upwind sand during the entire duration of both experiments. The vertical bed elevation changes were in the range of the ripple heights, of the order of a few millimeters.

For high wind conditions (later referred to as Regime II) in experiments S01, M01, and S02, a small amount of colored sand was eroded at the beginning of the experiments. After this initial erosion, native sand from the upwind direction deposited on top of the placement site, preventing the remaining colored sand from further movement. The observed sediment transport was mostly supplied from upwind source areas. The upwind sand cover on top of the tracer sand moved up and down due to phases of erosion and deposition (indicated in Figure 13 for S01), but the colored sand layer underneath was not re-exposed once it was fully covered by upwind sand. From the digitized side-view images during S01 (see Section 4), a total movement of the upwind sand cover of 2 cm was observed. For the experiments M01 and S02, a similar magnitude of vertical movement was found from erosion pins in the top-view images. The observed bed-level variability was much larger than during moderate wind conditions, which was in the range of millimeters.

The phases of erosion and deposition from experiment S01 are compared to wind direction and speed (Figure 13). The wind was blowing from WSW with an average direction of 256°. Fluctuations in

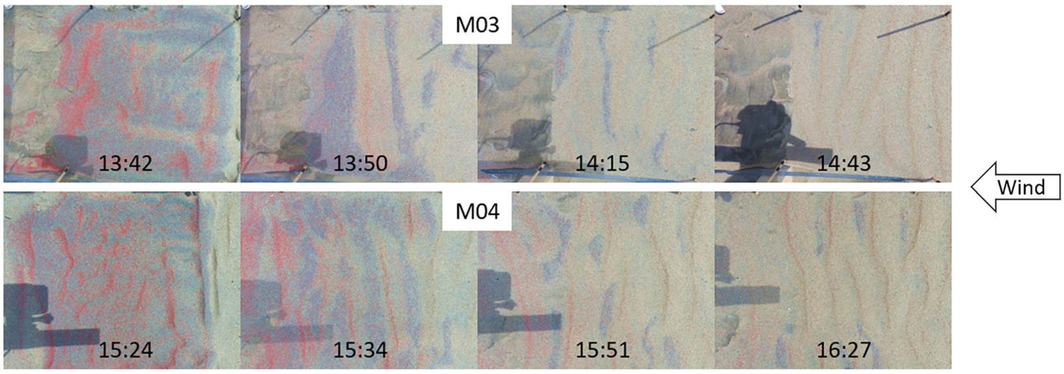

FIGURE 12 Vertical sorting of grain size fractions observed from the top-view Camera A images during moderate wind conditions (M03 and M04): coarser, red grains accumulated on the ripple crests, while a mix of finer, blue, green, and purple grains (which mix appears in the picture as dark-gray areas) accumulated in the ripple troughs. Patches of tracer sand underneath incoming upwind sand ripples are visible during the entire duration of both experiments, indicating a constant bed level

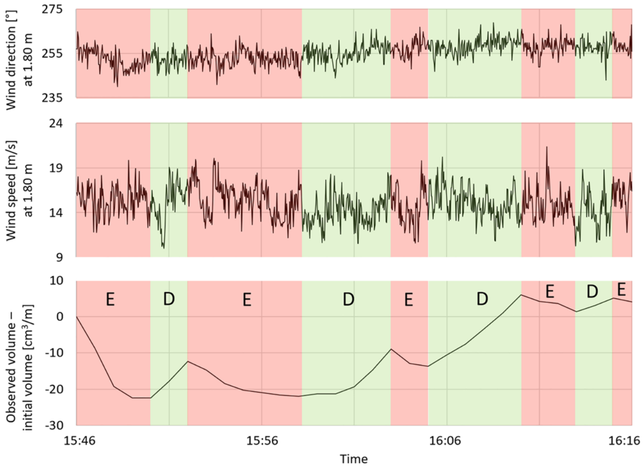

FIGURE 13 Wind direction and speed measured during high wind conditions (S01) at a frequency of 0.5 Hz and at a height of 1.80 m, and 1 min averaged volume difference between observed volume and initial volume at the placement site observed through the plexiglass screen. During the red intervals (E) sediment was eroded from the placement site, while during the green intervals (D) sediment was deposited

wind direction were small, within a range from 240° to 269°, and are therefore unlikely to influence the observed erosion and deposition phases. The wind speed fluctuated around an average of 15.1 m/s, with a maximum of 21.4 m/s and a minimum of 10 m/s. Theoretically, deposition would be expected in phases of decreasing wind speed and erosion during increasing wind speed. However, deposition was only observed during one period of decreasing wind speed, from 16:05 to 16:10. In contrast, from 15:52 to 15:57, erosion was observed during a period of decreasing wind speed. Performing linear regression analysis for 1 min averages in volume change and wind speed change results in a small coefficient of determination of $R^2 = 0.018$. This indicates that alternating phases of erosion and deposition of upwind sand were not directly correlated with gradients in the local wind speed.

4 | DISCUSSION

This field study provides new information and insights on the sediment sorting processes in time and space, the observation of bedform development during different wind speeds, the ripple migration speed, and the interaction between bedform development and transport of differently sized sediment. Here, these results are discussed in relation to previous research and aeolian transport models through a proposed conceptual model framework (Figure 14). The model framework aims to describe different aeolian transport regimes on sandy beaches, depending on wind forcing and grain size. Most sediment transport and the interaction between wind flow and sand particles occur at and near the sediment bed. In an effort to model aeolian sediment transport in this area at and near the sediment bed, we define the concept of an active bed surface layer (ABSL). The ABSL concept is similar to existing active layer concepts used to model river morphodynamics (e.g., Chavarrías et al., 2019; Hirano, 1971). We will use the ABSL concept to interpret the collected data during the fieldwork and we anticipate the use of the ABSL concept in future numerical model schematizations. Such an ABSL would, for instance, be compatible with the process-based model AeoLiS by Hoonhout and de Vries (2016), which already uses different layers for the bed discretizations.

4.1 | Definition of an active bed surface layer (ABSL)

The definition of the ABSL is based on both our field observations and literature. The ABSL includes the aeolian transport layer of grains in the creep and saltation mode, and the mobile/erodible bed described by its grain size and bedform characteristics. The mobile bed as part of the ABSL allows to account for both bedload transport and elevation changes due to erosion and deposition. Within the ABSL, grains can move between the mobile bed and the transport layer. In our experiments, we did not explicitly measure modes of transport, but only optically in the field and through the videos.

The upper boundary of the ABSL is the height to which the saltating particles can reach. The height of the aeolian saltation layer has been found to be independent of variations in wind speed but can be described as a function of the median particle diameter, d_{50} (Martin & Kok, 2017). Saltation heights are of the order of 150–200 times the d_{50}—that is, of the order of centimeters for sand-sized particles.

The lower boundary of the ABSL is at the boundary between the dynamic and static bed. The static bed is defined as having no changes in elevation or grain size characteristics during the timescale considered. Such a static bed was observed in all experiments and has also been observed in previous studies of Dutch beaches over the timescale of years (de Vries et al., 2015). The elevation of the static bed is assumed to be controlled by physical properties, such as grain size, surface moisture, and transport capacity. During the experiments, the 3 cm thick tracer sand layer was never completely eroded. Thus, for the prevailing conditions at the field site, the dynamic bed thickness was estimated to be of the order of centimeters.

4.2 | Sediment transport processes in the ABSL

Inspired by the work of Sherman et al. (2019) and Pye and Tsoar (2009), two transport regimes (I and II) with different transport and bedform characteristics are defined (Figure 14). The two regimes are distinguished based on the dimensionless wind shear velocity, u_*/u_{*t} (Sherman et al., 2019), incorporating both wind and sediment characteristics.

Regime I is defined for $1 < u_*/u_{*t} \leq 4$ and Regime II for $u_*/u_{*t} > 4$, corresponding to moderate and high wind speeds, respectively. The lower boundary of Regime I is the threshold velocity; when $u_*/u_{*t} \leq 1$, there is no sand transport in the ABSL. The boundary between Regime I and II, $u_*/u_{*t} = 4$, is based on bedform characteristics. When the threshold wind shear velocity is about three to four times the fluid threshold velocity, ripples disappear, and a planar surface is formed (Pye & Tsoar, 2009). Experiments M02, M03, M04, and

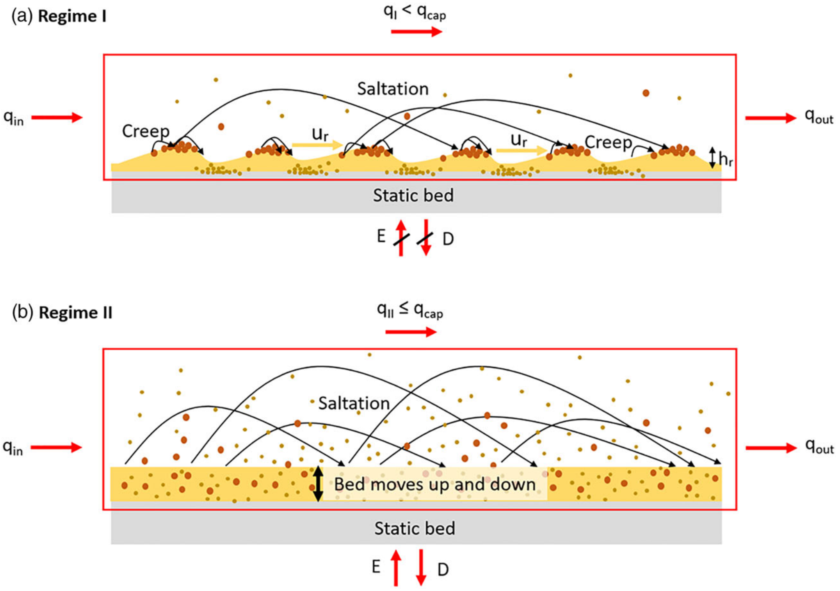

FIGURE 14 Schematic definition of the active bed surface layer (ABSL) modeling framework. The ABSL is defined by the red square. Transport processes are described for two regimes determined by wind speed and grain size characteristics. (a) Regime I: On top of a static bed (gray), ripples form as part of the ABSL with coarse grains (brown) at the ripple crests and finer grains (beige) in the ripple troughs. The ripples of height h_r move with a speed u_r. The supply of bed sediment for saltation is likely to be limited, causing the actual transport of Regime I, q_I, to be smaller than the sediment transport capacity by wind, q_{cap}. The vertical fluxes of erosion, E, and deposition, D, are assumed to be small.
(b) Regime II: On top of a static bed (gray), upwind sediment temporarily deposits, D, and erodes, E, causing the mobile bed of the ABSL to move up and down in the order of centimeters. Above the mobile bed layer, both fine (beige) and coarse (brown) grains move mainly in saltation. Sediment transport of Regime II, q_{II}, can be smaller than or equal to the sediment transport capacity by wind, q_{cap}

S03 are categorized as Regime I events, while M03, M04, and S03 are Regime II events (Figure 15).

In Regime I most transport in the ABSL takes place in close contact with the bed in the form of ripple movement, creep and saltation, whereas in Regime II most transport in the ABSL takes place in the form of saltation. It is assumed that the different transport characteristics influence the magnitude of aeolian sediment transport and thus require different modeling approaches.

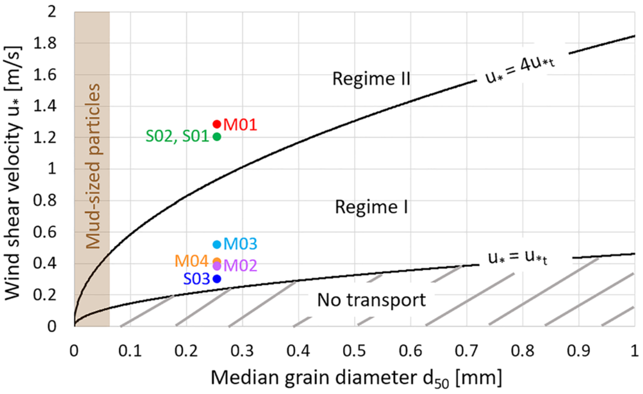

FIGURE 15 Regime classification based on median grain size and wind shear velocity. The striped gray area underneath the $u_* = u_{*t}$ line corresponds to no transport in the ABSL, the area between the $u_* = u_{*t}$ and $u_* = 4u_{*t}$ line corresponds to Regime I, and the area above the $u_* = 4u_{*t}$ line corresponds to Regime II. The colored dots indicate in which regime the experiments M01–M04 and S01–S03 lie. The regime classification is meant for sandy beaches and is thus not valid for beaches with mainly mud-sized particles (brown area on the left)

4.2.1 | Regime I

The results of experiments with moderate wind speeds (M03, M04, and S03) displayed the following characteristics associated with Regime I: (1) ripples formed with coarser grains on the ripple crests and smaller grains in the ripple troughs (see Figure 12); (2) ripples propagated in downwind direction with a linear relationship between dimensionless ripple propagation speed and dimensionless wind shear velocity (see Figure 11); (3) once ripples had formed, the supply of finer grains in the downwind direction decreased, while the supply of coarser grains stayed constant (see Figure 9).

Bagnold (1941) was one of the first who explained the formation of aeolian ripples due to the instability of a flat bed. From observations, he found that a flat sand surface must become unstable when sand grains saltate, since the saltation impacts are higher on the windward than on the leeward slopes of any small deformations of the bed surface. This explanation remains the basis of modern understanding of the initial stage of flat surface instability (Manukyan & Prigozhin, 2009). The subsequent formation of ripples and vertical sorting can be explained by the different transport trajectories of coarse and fine grains (Anderson & Bunas, 1993; Bagnold, 1941; Durán et al., 2011; Wang et al.2019). Smaller grains tend to saltate over the crest and reach the trough, or beyond it, before coming to rest, whereas the larger grains tend to stop at the crests immediately (Bagnold, 1941).

The observed ripple migration rates are similar to observations in previous studies. Sherman et al. (2019) compared observations from their field studies (Jericoacoara, Brazil, 2008, and Oceano, California,

2015) to ripple migrations by Sharp (1963) and Andreotti et al. (2006). They also found a linear relationship between dimensionless shear velocity and ripple speed, where $u_r/\sqrt{gd} = 0.0040(u_*/u_{*t} - 0.65)$ with $n = 161$ and $R^2 = 0.63$ (Sherman et al., 2019). Performing linear regression analysis for all data results in a relationship where $u_r/\sqrt{gd} = 0.0039(u_*/u_{*t} - 0.72)$ with $n = 192$ and $R^2 = 0.59$ (Figure 16). The threshold value for ripple movement for all data (0.72) is smaller compared to our data (1.49), which may be due to different environmental conditions during the experiments (e.g., temperature, beach slope, wind direction w.r.t. coastal orientation). Ripple movement speeds might be higher for warmer temperatures due to a likely smaller moisture content of the surface sands. Furthermore, ripple movement might also be faster for ripples traveling up mildly sloped beaches due to smaller gravity forces. The wind direction w.r.t. the beach orientation influences whether ripples travel up or down beach slopes: Ripples are likely to travel faster down beach slopes than up due to gravity. The wind direction w.r.t. the beach orientation also influences the fetch length and therefore the amount of saltating particles. Ripples might travel faster if a long fetch is available (e.g., alongshore winds) and thus more particles are saltating, which can cause further movement due to their impact/collision with particles on the ground. Compared to the other field observations, our ripple migration rates are consistently slower for the same dimensionless shear velocity.

To the best of our knowledge, the observed decrease of transport of the finer fractions after ripples formed (see Figure 9) has not previously been observed in the context of aeolian sediment transport. We hypothesize that the formation of ripples and the associated sediment sorting cause an armoring of the bed, which reduces sediment supply. The explaining mechanism could be that the asymmetric shape of aeolian ripples results in more impacts of saltating grains on the mildly sloped upwind side of the ripples than on the steeply sloped lee side (Bagnold, 1941; Kok et al., 2012; Sharp, 1963). Each collision of a saltating grain with the bed surface may result in the ejection of many creeping particles. At the upwind side of the ripples, which contains the crest, mainly coarser grains were found (see Figures 10 and 12). These coarser grains at the less steep upwind side of the ripples are highly impacted by saltating grains, which causes them to be set in motion and mainly be transported through creep in near-continuous contact with the sand bed. At the lee side of the ripples, which contains the trough, mainly finer grains were found (see Figures 10 and 12). These finer grains at the steep lee side of the ripples are less likely to be impacted by saltating grains, causing them to be sheltered and only occasionally start moving. This means that less sediment is supplied from the moving bed into the creep/saltation layer compared to a situation with a well-mixed, flat bed (Regime II).

For Regime I, sediment in the ABSL is partly transported as bedload in the form of ripples, q_r, with the ripple velocity, u_r, and height, h_r, and partly in the form of saltation, q_s. Further, it was observed that some individual grains moved as creep across ripple surfaces, q_c, faster than the ripple migration. Then, the total sediment flux for Regime I, q_I, is expressed through

$$q_I = q_r + q_s + q_c. \tag{5}$$

During experiments M03 and M04, no significant bed-level changes were observed. Thus it is assumed that all sediment entering the ABSL from the upwind direction leaves the ABSL in the downwind direction.

The mass of sand transported by ripple movement, q_r, can be estimated according to Jerolmack et al. (2006):

$$q_r = (1 - p)\rho_s u_r \frac{h_r}{2}, \tag{6}$$

where p is porosity of the bed. Assuming that variations in p, ρ_s, and h_r are small, the magnitude of ripple sediment transport depends on the ripple speed only. Thus the linear relationship between wind speed and ripple speed (Figure 11) can then be used for sediment transport predictions if the wind speed is known.

The saltation and creep sediment fluxes q_s and q_c can be estimated by relating ripple transport rates to total sand transport rates (Sherman et al., 2019), who found that q_r/q_I increases weakly with shear velocity, indicating that the proportion of q_r relative to the total sediment transport q_I is nearly constant. Defining $X = q_r/q_I$, the total sand transport rates can be related to ripple migration rates:

$$q_I = \frac{1}{X} q_r = \frac{1}{X}(1 - p)\rho_s u_r \frac{h_r}{2}. \tag{7}$$

Sherman et al. (2019) found that the proportion of ripple transport relative to the total transport averages $X = 0.036$ (standard deviation = 0.023). In this study, no sediment fluxes were directly measured. In future studies, it would be useful to design experiments that measure both sediment fluxes and ripple migration speeds to further investigate the proposed relationship.

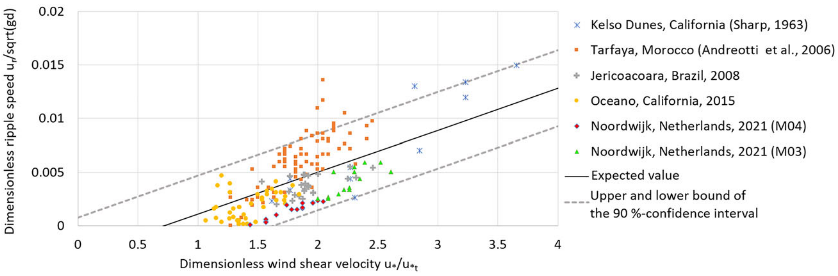

FIGURE 16 Dimensionless migration rates as a function of dimensionless shear velocity ($n = 192, R^2 = 0.59$). The solid line indicates the expected value from the regression model of all measurement points ($u_r/\sqrt{gd} = 0.0039(u_*/u_{*t} - 0.72)$). The dashed lines indicate the boundaries of the 90% confidence interval. For 10% of the measurements, the dimensionless ripple speed $u_r/\sqrt{gd}$ deviates more than 0.00356 from the expected value

Generally, for supply-limited situations, the actual sediment transport is smaller than the theoretical sediment transport capacity by wind, q_{cap} (Equation 1). Upscaling ripple sediment transport rates, q_r, to total sediment transport rates, q_I, by using a constant factor, X, would imply that sediment transport is linearly proportional to wind speed. A linear relationship between wind speed and total transport rates during supply-limited conditions is supported by previous research by de Vries et al. (2014).

4.2.2 | Regime II

The results of experiments S01, M01, and S02 displayed the following characteristics associated with Regime II: (1) no ripples were present; (2) different grain size fractions did not show distinct differences in transport rates (see Figure 7); (3) alternating phases of erosion and deposition of upwind sand were not directly correlated with gradients in the local wind speed (see Figure 13); (4) eroded and deposited volumes were of the same order of magnitude, so that the net bed level did not change over the course of the experiments (see Figure 13).

The absence of ripples in Regime II can be explained by the coarser sediment at the ripple crest observed in Regime I being brought into saltation (Pye & Tsoar, 2009). When the ripples lengthen and flatten out, the armor layer disintegrates, and previously sheltered particles become available for sediment transport. Consequently, no grain size-induced supply limitations are present, and the dominant sediment transport mode is simultaneous saltation of finer and coarser grains. However, the sediment in the static bed might be supply limited due to other factors, such as moisture.

Aeolian sediment transport models typically relate transport and bed-level changes to changes in wind speed (e.g., Kroy et al., 2002; Sauermann et al., 2001; Werner, 1990). However, in the Regime II experiments, the alternating phases of erosion and deposition could not be directly related to the local wind speed. The transported sediment, originating from an upwind sediment source, appeared to be deposited on a static bed. Previous research observed similar behavior and related temporal variations in sediment transport fluxes not only to temporal changes in wind speed, but also to temporal changes in upwind sediment supply (de Vries et al., 2013, 2014). Temporal variations in upwind sediment supply can, for example, occur due to the interaction between marine and aeolian processes in the intertidal zone. In order to simulate bed-level changes in the area between the intertidal zone and the dune toe, temporal changes of upwind sediment supply next to temporal variations in wind-driven transport capacity should be taken into account. The area between the intertidal zone and the dune toe then functions as a pathway for sediment from upwind sources and undergoes bed-level fluctuations above the static bed in alternating phases of erosion and deposition.

The phases of erosion and deposition can be explained using an Exner (1920)-style approach by a sediment balance of the ABSL. In case $q_{in} < q_{out}$ sediment erodes from the active bed ($E - D > 0$) and in case $q_{in} > q_{out}$ sediment accretes ($E - D < 0$). For $q_{in} = q_{out}$ the bed is constant. Temporary deposition occurs when the transport capacity by wind is reached, $q_{II} = q_{cap}$. The transport capacity can be estimated by a third power relationship to the wind speed—for example, the Bagnold equation (Equation 1). Temporary erosion occurs when $q_{II} < q_{cap}$. Additional sediment is then added to the saltation/creep layer from the mobile bed. To account for spatiotemporal variations in wind speed and supply limitations, both the transport capacity (Equation 1) and the upwind sediment supply should be taken into account. A process-based area model such as AeoLiS (Hoonhout & de Vries, 2016), simulating spatiotemporal variations in bed surface properties and sediment availability, could be adopted for this purpose.

4.3 | Outlook for the application of the ABSL

We explored the concept of an ABSL that can support aeolian sediment transport modeling efforts, including the effects of wind speed, sediment supply, and bed characteristics such as grain size and bedforms. The conceptual model framework is based on our observations of sediment transport and sorting in the interaction zone between the bed and the moving air. The conceptual model framework differentiates between two regimes for different transport characteristics and proposes different modeling approaches for these two regimes to estimate aeolian sediment transport rates in coastal environments. The two regimes are defined based on the dimensionless wind shear velocity, u_* / u_{*t}, which allows for comparison of results from other research studies and enables new empirical findings to be placed in a context.

The proposed concepts are mainly based on observations from one beach—Noordwijk in the Netherlands—and only from the supratidal area. Future work should focus on investigating the transferability of these results to other beach environments and expanding the conceptual model by introducing limiting factors, such as moisture. Moisture may influence both the threshold for transport, but also bed characteristics. Nield et al. (2011) found that, after rainfall, adhesion structures developed that were much larger than ripples. Due to their different dimensions, they might influence aeolian sediment transport differently from ripples and be described as an additional transport regime.

Existing numerical area models—for example those by Hoonhout and de Vries (2016) and Durán and Moore (2013)—do not yet account for complex interactions between the sediment bed and the wind. The ABSL framework could be introduced in these models to account for the supply-limiting effects of bedforms. The ABSL can also be applied to prevent the simulation of unrealistic erosion patterns by introducing the static bed concept. However, for this purpose, a quantitative description of the static bed would be required. Future research could investigate the feasibility of hydrodynamic concepts that define a vertical limit to bed movement based on physical or modeling considerations in the aeolian environment, such as the concept of depth of disturbance (DoD) (King, 1951) or sediment layers with source–sink exchange (SILKE) (Chavarrías et al. 2019).

The tracer study is a promising method to investigate sorting processes and increase the knowledge base for the ABSL. However, the experimental setup used for this tracer study is not feasible for estimates of sediment fluxes. Future tracer field studies can benefit from combining qualitative tracer observation with quantitative flux measurements. However, aeolian process measurements generally lack a standardized method to compare measurements from one study to another (Barchyn et al., 2011). The most common methods to measure aeolian sediment transport are sediment traps, saltiphones, and laser sensors (van Rijn, 2019), which are all point measurement methods. The introduction of standardized methods for some of these point measurement instruments has, for example, been addressed by Ellis et al. (2009) by providing a protocol for the use of sediment traps. However, no method for measuring aeolian sediment fluxes is widely applied and accepted in the aeolian community yet. Future research should focus on collecting more comparable data by adopting the methods to the standardized protocol. Additionally, more standardized protocols for different aeolian sediment transport measurement methods should be established to overcome comparison problems between different studies and to allow a more quantitative interpretation of measurement results.

5 | CONCLUSIONS

A set of field experiments with tracers was carried out on the supratidal beach at Noordwijk, the Netherlands, to improve our understanding of aeolian grain-size-selective transport on beaches. The novel field study technique using colored grain size fractions and automated pixel-color recognition resulted in several observations of sorting, bedform, and transport processes. During moderate wind conditions, the tracer sand interacted with the sediment entering the test site from the upwind direction, forming aeolian ripples with coarser grains on the ripple crests and finer grains in the ripple troughs. Once the ripples formed, the supply of finer tracer grains in the downwind direction decreased over time, while the supply of coarser grains remained constant. A linear relationship between dimensionless ripple propagation speed and dimensionless wind shear velocity was found. For higher wind velocities, no ripples or differences in transport of different grain sizes in downwind direction were observed. Temporally-varying phases of erosion and deposition of up to 2 cm upwind sand were observed, which could not be related to local gradients in wind speed.

The observations were translated into a conceptual framework for modeling aeolian transport, erosion, and deposition at the bed surface through the concept of an active bed surface layer (ABSL). The most important characteristics of the ABSL are explained for two transport regimes corresponding to moderate (I) and high (II) wind speeds. The dimensionless wind shear velocity, defined as the ratio of wind shear velocity, u_*, over wind shear threshold velocity, u_{*t}, is used to distinguish between the regimes. The two regimes can be distinguished based on their different characteristics.

In Regime I ($1 < u_*/u_{*t} \leq 4$), ripples form as part of the ABSL. Sediment is sorted with coarser grains at the ripple crests and finer grains in the ripple troughs. The sorting and partly sheltering of the finer sediment limit the supply of sediment from the bed. Sediment is partly transported as bedload in the form of ripples, which scales linearly with wind speed, and partly transported above the bed in the form of creep and saltation. We propose to upscale the linear relationship between ripple transport and wind speed to make total sediment transport predictions for Regime I by using a constant value for the proportion of ripple transport compared to total transport according to Sherman et al. (2019). This would mean that total sediment transport is linearly proportional to wind speed, which is less strong than a third power relationship for aeolian sediment transport capacity.

In Regime II ($u_*/u_{*t} > 4$), the dynamics of the ABSL are mainly influenced by the supply of upwind sediment and spatiotemporal variations in wind speed. Possibly, temporally varying gradients in upwind sediment supply and wind speed result in temporal phases of erosion and deposition. A third power relationship between sediment transport and wind speed in combination with a process-based model that accounts for supply limitations seems suitable for making aeolian sediment transport predictions for Regime II. The time average of the eroding and accreting phases seems to be very small, which indicates that the considered beach area functions as a pathway for sediment eroded from upwind areas rather than as a source for aeolian sediment itself.

The ABSL concept helps to better quantify aeolian sediment transport by focusing on the most important processes in the ABSL and by using different transport regimes for different wind speeds. We therefore anticipate the use of the ABSL concept in future numerical model schematizations.

ACKNOWLEDGEMENTS

This research would not have been possible without the equipment, assistance, and support of the TU Delft Hydraulic Engineering Laboratory, especially Pieter van der Gaag, Chantal Willems, and Arno Doorn. We would like to thank Ines Kodde (Wageningen University), Michiel Smit (TU Delft), and David Hart, who came out to help Charlotte Uphues during fieldwork. We also acknowledge the surf school 'Beach Break' for providing their facilities at Noordwijk beach, the Netherlands, during fieldwork.

AUTHOR CONTRIBUTIONS

All authors took part in the conceptualization of the research. The methodology was developed by CU, CvIJ, CH, SP, and SdV. All data was collected, processed, and analyzed by CU. During the project, CvIJ, CH, SP, BvP, GMdS, and SdV acted as supervisors of CU. The initial draft was created by CU and all authors took part in reviewing and editing the final manuscript.

DATA AVAILABILITY STATEMENT

The data that support the findings of this study are available from the corresponding author upon reasonable request.

ORCID

Charlotte F. K. Uphues https://orcid.org/0000-0002-2079-9724
Christa O. van IJzendoorn https://orcid.org/0000-0001-9756-1856
Stuart G. Pearson https://orcid.org/0000-0002-3986-4469
Sierd de Vries https://orcid.org/0000-0001-5865-3715

REFERENCES

Anderson R.S. (1986) Sediment transport by wind: saltation, suspension, erosion and ripples. Ph.D. Thesis, University of Washington.

Anderson R.S., Bunas K.L. (1993) Grain size segregation and stratigraphy in aeolian ripples modelled with a cellular automaton. *Nature*, 365(6448), 740–743.

Andreotti B., Claudin P., Pouliquen O. (2006) Aeolian sand ripples: Experimental study of fully developed states. *Physical Review Letters*, 96, 28001. https://link.aps.org/doi/10.1103/PhysRevLett.96.028001

Bagnold R.A. (1935) The movement of desert sand. *The Geographical Journal*, 85(4), 342–365. http://www.jstor.org/stable/1785593

Bagnold R.A. (1937) The transport of sand by wind. *The Geographical Journal*, 89(5), 409–438. http://www.jstor.org/stable/1786411

Bagnold R.A. (1941) *The Physics of Blown Sand and Desert Dunes*. Chapman & Hall: London.

Bagnold R.A., Taylor G.I. (1937) The size-garding of sand by wind. *Proceedings of the Royal Society of London. Series A - Mathematical and Physical Sciences*, 163(913), 250–264. https://royalsocietypublishing.org/doi/abs/10.1098/rspa.1937.0225

Barchyn T.E., Hugenholtz C.H., Ellis J.T. (2011) A call for standardization of aeolian process measurements: moving beyond relative case studies. *Earth Surface Processes and Landforms*, 36(5), 702–705. https://onlinelibrary.wiley.com/doi/abs/10.1002/esp.2136

Barchyn T.E., Martin R.L., Kok J.F., Hugenholtz C.H. (2014) Fundamental mismatches between measurements and models in aeolian sediment transport prediction: The role of small-scale variability. *Aeolian Research*, 15, 245–251.

Bauer B.O., Davidson-Arnott R. G. D. (2003) A general framework for modeling sediment supply to coastal dunes including wind angle, beach geometry, and fetch effects. *Geomorphology*, 49(1), 89–108. https://www.sciencedirect.com/science/article/pii/S0169555X02001654

Berg N.H. (1983) Field evaluation of some sand transport models. *Earth Surface Processes and Landforms*, 8(2), 101–114. https://onlinelibrary.wiley.com/doi/abs/10.1002/esp.3290080202

Black K., Athey S., Wilson P., Evans D. (2007) The use of particle tracking in sediment transport studies: A review. *Geological Society, London, Special Publications*, 274, 73–91.

Black K., Poleykett J., Uncles R.J., Wright M.R. (2017) Sediment transport: Instrumentation and methodologies. In *Estuarine and Coastal Hydrography and Sediment Transport*, Cambridge University Press; 261–292.

Buckley R. (1987) The effect of sparse vegetation on the transport of dune sand by wind. *Nature*, 325(6103), 426–428.

Cabrera L.L., Alonso I. (2010) Correlation of aeolian sediment transport measured by sand traps and fluorescent tracers. *Journal of Marine Systems*, 80(3), 235–242. https://www.sciencedirect.com/science/article/pii/S0924796309003005, Models and observations of Marine Systems.

Charnock H. (1955) Wind stress on a water surface. *Quarterly Journal of the Royal Meteorological Society*, 81(350), 639–640. https://rmets.onlinelibrary.wiley.com/doi/abs/10.1002/qj.49708135027

Chavarrías V., Arkesteijn L., Blom A. (2019) A well-posed alternative to the hirano active layer model for rivers with mixed-size sediment. *Journal of Geophysical Research: Earth Surface*, 124(11), 2491–2520. https://agupubs.onlinelibrary.wiley.com/doi/abs/10.1029/2019JF005081

Davidson-Arnott R. G. D., MacQuarrie K., Aagaard T. (2005) The effect of wind gusts, moisture content and fetch length on sand transport on a beach. *Geomorphology*, 68(1), 115–129. https://www.sciencedirect.com/science/article/pii/S0169555X04002922, Fluid Flow and Sediment Transport Process in Geomorphology.

de Vries S., Arens S.M., de Schipper M. A., Ranasinghe R. (2014) Aeolian sediment transport on a beach with a varying sediment supply. *Aeolian Research*, 15, 235–244. https://www.sciencedirect.com/science/article/pii/S1875963714000615

de Vries S., Harley M.D., de Schipper M. A., Ruessink G. (2015) Dune growth due to aeolian sedimenttransport and the role of the beach and intertidal zone. In: Wang P., Rosati J. D. & Cheng J. (Eds.) *Coastal Sediments 2015: The Proceedings of the Coastal Sediments 2015. World Scientific*, pp. 1–14. https://doi.org/10.1142/9789814689977_0043

de Vries S., Southgate H.N., Kanning W., Ranasinghe R. (2012) Dune behavior and aeolian transport on decadal timescales. *Coastal Engineering*, 67, 41–53. https://www.sciencedirect.com/science/article/pii/S0378383912000725

de Vries S., van Thiel de Vries J., Ruessink G. (2013) Modelling aeolian sediment accumulations on a beach (pp. 511–520).

de Vries S., van Thiel de Vries J. S. M., van Rijn L. C., Arens S.M., Ranasinghe R. (2014) Aeolian sediment transport in supply limited situations. *Aeolian Research*, 12, 75–85. https://www.sciencedirect.com/science/article/pii/S1875963713000992

Durán O., Moore L.J. (2013) Vegetation controls on the maximum size of coastal dunes. *Proceedings of the National Academy of Sciences*, 110(43), 17217–17222. https://www.pnas.org/content/110/43/17217

Durán O., Claudin P., Andreotti B. (2011) On aeolian transport: Grain-scale interactions, dynamical mechanisms and scaling laws. *Aeolian Research*, 3(3), 243–270. https://www.sciencedirect.com/science/article/pii/S1875963711000632

Ellis J.T., Li B., Farrell E.J., Sherman D.J. (2009) Protocols for characterizing aeolian mass-flux profiles. *Aeolian Research*, 1(1), 19–26. https://www.sciencedirect.com/science/article/pii/S1875963709000020

Exner F.M. (1920) Zur Physik der Dünen. *Sitzungsberichte der Akademie der Wissenschaften in Wien, Abt. IIa, Band*, 129, 929–952. (in German).

Hardisty J., Whitehouse R. J. S. (1988) Evidence for a new sand transport process from experiments on saharan dunes. *Nature*, 332(6164), 532–534.

Hirano M. (1971) River-bed degradation with armouring, Proceedings of the Japan Society of Civil Engineers, Japan Society of Civil Engineers.

Hoonhout B., de Vries S. (2016) A process-based model for aeolian sediment transport and spatiotemporal varying sediment availability. *Journal of Geophysical Research: Earth Surface*, 121(8), 1555–1575.

Hoonhout B., de Vries S. (2017) Field measurements on spatial variations in aeolian sediment availability at the sand motor mega nourishment. *Aeolian Research*, 24, 93–104. https://www.sciencedirect.com/science/article/pii/S1875963716301264

Houser C. (2009) Synchronization of transport and supply in beach-dune interaction. *Progress in Physical Geography*, 33, 733–746.

Hsu S.-A. (1971) Wind stress criteria in eolian sand transport. *Journal of Geophysical Research (1896-1977)*, 76(36), 8684–8686. https://agupubs.onlinelibrary.wiley.com/doi/abs/10.1029/JC076i036p08684

Jerolmack D.J., Mohrig D., Grotzinger J.P., Fike D.A., Watters W.A. (2006) Spatial grain size sorting in eolian ripples and estimation of wind conditions on planetary surfaces: Application to meridiani planum, mars. *Journal of Geophysical Research: Planets* 111(E12), 1–14. https://agupubs.onlinelibrary.wiley.com/doi/abs/10.1029/2005JE002544

Kato S., Okabe T., Aoki Y., Kamohara S. (2014) Field measurement of sand movement on river-mouth tidal flat using color sand tracing. *Coastal Engineering Proceedings*, 1(34), 61. https://journals.tdl.org/icce/index.php/icce/article/view/7669

Kawamura R. (1951) Study on sand movement by wind. *Annual Report Institute Science and Technology*, 5, 95–112.

Keyence Corporation (2014) *Vhx-5000 digital microscope user's manual*. Keyence Corporation. http://uhulag.mendelu.cz/files/pagesdata/cz/biometrickalaborator/vhx-5000_user-manual.pdf

King C. A. M. (1951) Depth of disturbance of sand on sea beaches by waves. *Journal of Sedimentary Research*, 21(3), 131–140. https://doi.org/10.1306/D4269445-2B26-11D7-8648000102C1865D

Kok J., Parteli E., Michaels T., Francis D. (2012) The physics of wind-blown sand and dust. *Reports on Progress in Physics. Physical Society (Great Britain)*, 75, 106901.

Kroon A., Hoekstra P. (1990) Eolian sediment transport on a natural beach. *Journal of Coastal Research*, 6(2), 367–379.

Kroy K., Sauermann G., Herrmann H.J. (2002) Minimal model for sand dunes. *Physical Review Letters*, 88, 54301. https://link.aps.org/doi/10.1103/PhysRevLett.88.054301

Lettau K., Lettau H. (1978) Experimental and micrometeorological field studies of dune migration. In *Exploring the world's driest climate*, Lettau H. H., Lettau K. (eds), IES Report 101; 110–147.

Manukyan E., Prigozhin L. (2009) Formation of aeolian ripples and sand sorting. *Physical Review. E, Statistical, Nonlinear, and Soft Matter Physics*, 79, 31303.

Martin R., Kok J. (2017) Wind-invariant saltation heights imply linear scaling of aeolian saltation flux with shear stress. *Science Advances*, 3(6), e1602569.

Nickling W., Davidson-Arnott R. (1990) Aeolian sediment transport on beaches and coastal sand dunes.

Nield J.M., Wiggs G. F. S., Squirrell R.S. (2011) Aeolian sand strip mobility and protodune development on a drying beach: Examining surface moisture and surface roughness patterns measured by terrestrial laser scanning. *Earth Surface Processes and Landforms*, 36(4), 513–522. https://onlinelibrary.wiley.com/doi/abs/10.1002/esp.2071

Oliveira S., Moura D., Horta J., Nascimento A., Gomes A., Veiga-Pires C. (2017) The morphosedimentary behaviour of a headland-beach system: Quantifying sediment transport using fluorescent tracers. *Marine Geology*, 388, 62–73. https://www.sciencedirect.com/science/article/pii/S0025322716302274

Owen P.R. (1964) Saltation of uniform grains in air. *Journal of Fluid Mechanics*, 20, 225–242.

Pähtz T., Clark A.H., Valyrakis M., Durán O. (2020) The physics of sediment transport initiation, cessation, and entrainment across aeolian and fluvial environments. *Reviews of Geophysics*, 58(1), e2019RG000679. https://agupubs.onlinelibrary.wiley.com/doi/abs/10.1029/2019RG000679

Pähtz T., Parteli E. J. R., Kok J.F., Herrmann H.J. (2014) Analytical model for flux saturation in sediment transport. *Physical Review E*, 89, 52213. https://link.aps.org/doi/10.1103/PhysRevE.89.052213

Pearson S.G., van Prooijen B. C., Poleykett J., Wright M., Black K., Wang Z. B. (2021) Tracking fluorescent and ferrimagnetic sediment tracers on an energetic ebb-tidal delta to monitor grain size-selective dispersal. *Ocean and Coastal Management*, 212, 105835.

Pye K., Tsoar H. (2009) Aeolian bed forms. In *Aeolian sand and sand dunes*, Springer Berlin Heidelberg: Berlin, Heidelberg; 175–253. https://doi.org/10.1007/978-3-540-85910-9_6

Quartel S., Ruessink B.G., Kroon A. (2007) Daily to seasonal cross-shore behaviour of quasi-persistent intertidal beach morphology. *Earth Surface Processes and Landforms*, 32(9), 1293–1307. https://onlinelibrary.wiley.com/doi/abs/10.1002/esp.1477

Robin N., Levoy F., Monfort O. (2009) Short term morphodynamics of an intertidal bar on megatidal ebb delta. *Marine Geology*, 260(1), 102–120. https://www.sciencedirect.com/science/article/pii/S0025322709000401

Sarre R.D. (1989) Aeolian sand drift from the intertidal zone on a temperate beach: Potential and actual rates. *Earth Surface Processes and Landforms*, 14(3), 247–258.

Sauermann G., Kroy K., Herrmann H.J. (2001) Continuum saltation model for sand dunes. *Physical Review E*, 64, 31305. https://link.aps.org/doi/10.1103/PhysRevE.64.031305

Schmutz P.P., Namikas S.L. (2018) Measurement and modeling of the spatiotemporal dynamics of beach surface moisture content. *Aeolian Research*, 34, 35–48. https://www.sciencedirect.com/science/article/pii/S187596371830106X

Sharp R.P. (1963) Wind ripples. *The Journal of Geology*, 71(5), 617–636. https://doi.org/10.1086/626936

Sherman D.J., Farrell E.J. (2008) Aerodynamic roughness lengths over movable beds: Comparison of wind tunnel and field data. *Journal of Geophysical Research: Earth Surface* 113(F2). https://agupubs.onlinelibrary.wiley.com/doi/abs/10.1029/2007JF000784

Sherman D.J., Jackson D. W. T., Namikas S.L., Wang J. (1998) Wind-blown sand on beaches: An evaluation of models. *Geomorphology*, 22(2), 113–133. https://www.sciencedirect.com/science/article/pii/S0169555X97000627, Aeolian Environments.

Sherman D.J., Li B. (2012) Predicting aeolian sand transport rates: A reevaluation of models. *Aeolian Research*, 3(4), 371–378. https://www.sciencedirect.com/science/article/pii/S1875963711000449, The 7th International Conference on Aeolian Research (ICAR VII), Santa Rosa, Argentina.

Sherman D.J., Li B., Ellis J.T., Farrell E.J., Maia L.P., Granja H. (2013) Recalibrating aeolian sand transport models. *Earth Surface Processes and Landforms*, 38(2), 169–178. https://onlinelibrary.wiley.com/doi/abs/10.1002/esp.3310

Sherman D.J., Zhang P., Martin R.L., Ellis J.T., Kok J.F., Farrell E.J., Li B. (2019) Aeolian ripple migration and associated creep transport rates. *Geosciences*, 9(9), 389. https://www.mdpi.com/2076-3263/9/9/389

Silva A., Taborda R., Rodrigues A., Duarte J., Cascalho J. (2007) Longshore drift estimation using fluorescent tracers: New insights from an experiment at comporta beach, portugal. *Marine Geology*, 240, 137–150.

Sørensen M. (2004) On the rate of aeolian sand transport. *Geomorphology*, 59(1), 53–62. https://www.sciencedirect.com/science/article/pii/S0169555X03003131, Aeolian Research: processes, instrumentation, landforms and palaeoenvironments.

Tennekes H., Lumley J.L. (1972) *A First Course in Turbulence*. The MIT Press. https://doi.org/10.7551/mitpress/3014.001.0001

Tsoar H., Pye K. (1987) Dust transport and the question of desert loess formation. *Sedimentology*, 34(1), 139–153. https://onlinelibrary.wiley.com/doi/abs/10.1111/j.1365-3091.1987.tb00566.x

van Rijn L. C. (2014) A simple general expression for longshore transport of sand, gravel and shingle. *Coastal Engineering*, 90, 23–39. https://www.sciencedirect.com/science/article/pii/S0378383914000787

van Rijn L. C. (2019) Aeolian transport over a flat sediment surface. https://www.leovanrijn-sediment.com

van der Wal D. (1998) Effects of fetch and surface texture on aeolian sand transport on two nourished beaches. *Journal of Arid Environments*, 39(3), 533–547. https://www.sciencedirect.com/science/article/pii/S0140196397903645

Vila-Concejo A., Óscar Ferreira, Ciavola P., Matias A., Dias J. M. A. (2004) Tracer studies on the updrift margin of a complex inlet system. *Marine Geology*, 208(1), 43–72. https://www.sciencedirect.com/science/article/pii/S0025322704001203

Walker J.D. (1981) An Experimental Study of Wind Ripples. Master's Thesis, Massachusetts Institute of Technology, Cambridge, MA, USA.

Walstra D. J. R., Reniers A. J. H. M., Ranasinghe R., Roelvink J.A., Ruessink B.G. (2012) On bar growth and decay during interannual net offshore migration. *Coastal Engineering*, 60, 190–200. https://www.sciencedirect.com/science/article/pii/S0378383911001682

Wang G., Li J., Ravi S., Scott Van Pelt R., Costa P. J. M., Dukes D. (2017) Tracer techniques in aeolian research: Approaches, applications, and challenges. *Earth-Science Reviews*, 170, 1–16. https://www.sciencedirect.com/science/article/pii/S0012825217300466

Wang P., Zhang J., Huang N. (2019) A theoretical model for aeolian polydisperse-sand ripples. *Geomorphology*, 335, 28–36. https://www.sciencedirect.com/science/article/pii/S0169555X19301060

Werner B.T. (1990) A steady-state model of wind-blown sand transport. *Journal of Geology*, 98(1), 1–17. cited By 195.

White T.E. (1998) Status of measurement techniques for coastal sediment transport. *Coastal Engineering*, 35(1), 17–45. https://www.sciencedirect.com/science/article/pii/S0378383998000337

Wijnberg K.M., Terwindt J. H. J. (1995) Extracting decadal morphological behaviour from high-resolution, long-term bathymetric surveys along the holland coast using eigenfunction analysis. *Marine Geology*, 126(1), 301–330. https://www.sciencedirect.com/science/article/pii/002532279500084C

Williams J.J., O'Connor B.A., Arens S.M., Abadie S., Bell P., Balouin Y., Boxel J. H. V., Carmo A. J. D., Davidson M., Ferreira O., Heron M., Howa H., Hughes Z., Kaczmarek L.M., Kim H., Morris B., Nicholson J., Pan S., Salles P., Silva A., Smith J., Soares C., Vila-Concejo A.. 2003. Tidal inlet function: Field evidence and numerical simulation in the india project. *Journal of Coastal Research* 19(1): 189–211. http://www.jstor.org/stable/4299157

Wilson I.G. (1972) Aeolian bedforms - their development and origins. *Sedimentology*, 19(3-4), 173–210. https://onlinelibrary.wiley.com/doi/abs/10.1111/j.1365-3091.1972.tb00020.x

Wright M., Poleykett J., Black K. (2015) P1486.03.05.d01v92 - scarborough south bay sand tracking (final report), partrac.

Zingg A.W. (1953) Wind tunnel studies of the movement of sedimentary material, Proceedings, 5th Hydraulics Conference, Studies in Engineering.

SUPPORTING INFORMATION

Additional supporting information can be found online in the Supporting Information section at the end of this article.

How to cite this article: Uphues, C.F.K., van IJzendoorn, C.O., Hallin, C., Pearson, S.G., van Prooijen, B.C., Miot da Silva, G. et al. (2022) Coastal aeolian sediment transport in an active bed surface layer: Tracer study and conceptual model. *Earth Surface Processes and Landforms*, 1–16. Available from: https://doi.org/10.1002/esp.5449